AIP Journal of Applied Physics

Pressure-assisted fabrication of organic light emitting diodes with MoO3 hole-injection layer materials

J. Du, V. C. Anye, E. O. Vodah, T. Tong, M. G. Zebaze Kana, and W. O. Soboyejo

Citation: Journal of Applied Physics **115**, 233703 (2014); doi: 10.1063/1.4881780
View online: http://dx.doi.org/10.1063/1.4881780
View Table of Contents: http://scitation.aip.org/content/aip/journal/jap/115/23?ver=pdfcov
Published by the AIP Publishing

Articles you may be interested in

Investigation of hole injection enhancement by MoO3 buffer layer in organic light emitting diodes
J. Appl. Phys. **114**, 244505 (2013); 10.1063/1.4852835

Barrierless hole injection through sub-bandgap occupied states in organic light emitting diodes using substoichiometric MoOx anode interfacial layer
Appl. Phys. Lett. **100**, 013311 (2012); 10.1063/1.3673283

MoO3 as combined hole injection layer and tapered spacer in combinatorial multicolor microcavity organic light emitting diodes
Appl. Phys. Lett. **99**, 093305 (2011); 10.1063/1.3623482

Enhancement of current injection in organic light emitting diodes with sputter treated molybdenum oxides as hole injection layers
Appl. Phys. Lett. **98**, 173302 (2011); 10.1063/1.3579532

Marked improvement in electroluminescence characteristics of organic light-emitting diodes using an ultrathin hole-injection layer of molybdenum oxide
J. Appl. Phys. **104**, 054501 (2008); 10.1063/1.2974089

Re-register for Table of Content Alerts

Create a profile.

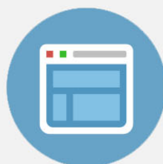

Sign up today!

[This article is copyrighted as indicated in the article. Reuse of AIP content is subject to the terms at: http://scitation.aip.org/termsconditions. Downloaded to] IP: 64.54.217.125 On: Tue, 17 Jun 2014 17:57:03

JOURNAL OF APPLIED PHYSICS 115, 233703 (2014)

Pressure-assisted fabrication of organic light emitting diodes with MoO_3 hole-injection layer materials

J. Du,[1,2] V. C. Anye,[3] E. O. Vodah,[3] T. Tong,[1,4] M. G. Zebaze Kana,[5,6] and W. O. Soboyejo[1,2,3]
[1]The Princeton Institute for the Science and Technology of Materials (PRISM), Princeton, New Jersey 08544, USA
[2]Department of Mechanical and Aerospace Engineering, Princeton University, Princeton, New Jersey 08544, USA
[3]Department of Materials Science and Engineering, African University of Science and Technology, Abuja, Federal Capital Territory, Nigeria
[4]Department of Electrical Engineering, Princeton University, Princeton, New Jersey 08544, USA
[5]Physics Advanced Laboratory, Sheda Science and Technology Complex, Abuja, Federal Capital Territory, Nigeria
[6]Department of Materials Science and Engineering, Kwara State University, Kwara State, Nigeria

(Received 6 January 2014; accepted 24 May 2014; published online 17 June 2014)

In this study, pressures of ~5 to ~8 MPa were applied to organic light emitting diodes containing either evaporated molybdenum trioxide (MoO_3) or spin-coated poly(3,4-ethylene dioxythiophene) doped with poly(styrene sulphonate) (PEDOT:PSS) hole-injection layers (HILs). The threshold voltages for both devices were reduced by about half, after the application of pressure. Furthermore, in an effort to understand the effects of pressure treatment, finite element simulations were used to study the evolution of surface contact between the HIL and emissive layer (EML) under pressure. The blister area due to interfacial impurities was also calculated. This was shown to reduce by about half, when the applied pressures were between ~5 and 8 MPa. The finite element simulations used Young's modulus measurements of MoO_3 that were measured using the nanoindentation technique. They also incorporated measurements of the adhesion energy between the HIL and EML (measured by force microscopy during atomic force microscopy). Within a fracture mechanics framework, the implications of the results are then discussed for the pressure-assisted fabrication of robust organic electronic devices. © *2014 AIP Publishing LLC*. [http://dx.doi.org/10.1063/1.4881780]

I. INTRODUCTION

Organic light emitting diodes (OLEDs) are layered structures that usually consist of successive organic layers that are stacked between a metallic cathode and an inorganic anode[1] (Fig. 1). The diode is usually built on a transparent substrate (such as glass) that eventually forms the display through which the emitted light is observed. On top of this substrate, there is a layer of highly conductive and transparent indium tin oxide (ITO), which forms the anode of the diode. Above the ITO anode, there is a thin layer of material that is used to facilitate hole-injection from the anode into the active layer. In most cases, poly(3,4-ethylene dioxythiophene) doped with poly(styrene sulphonate) (PEDOT:PSS) is widely used as a hole-injection layer (HIL) material. Next, the emissive layer (EML) of the OLED is deposited. To complete the diodes, conventional shadow masks are used to deposit a patterned aluminum layer to form the cathode.

However, the widely used hole-injection layer material, PEDOT:PSS, is not chemically stable.[2] The chemical reactions that occur at the interfaces between PEDOT:PSS and other layer can result in degradation of the OLEDs.[2] Also, its relatively limited work function hinders charge injection into organic materials with large ionization energy.[3] This has stimulated recent interest in the potential applications of transition metal oxides (TMOs), such as molybdenum trioxide (MoO_3), tungsten trioxide (WO_3), nickel oxide (NiO), or vanadium pentoxide (V_2O_5), as potential candidates to replace PEDOT:PSS in OLEDs,[4–6] organic photovoltaic (OPV) cells,[2,7] and organic thin film transistors (OTFT).[8] As novel HIL materials, TMOs can minimize charge injection barriers at organic semiconductor interfaces.[9] Hence, TMOs can lower operating voltages, while improving device efficiency. Furthermore, they have good optical transparency in the visible range, moderate conductivity, and low thermal evaporation temperature.[9]

A number of researchers[10–16] have studied the effects of pressure on the fabrication and performance of organic electronic devices. Kim *et al.*[10] observed that OLEDs fabricated after pressure treatment exhibited a notable increase in

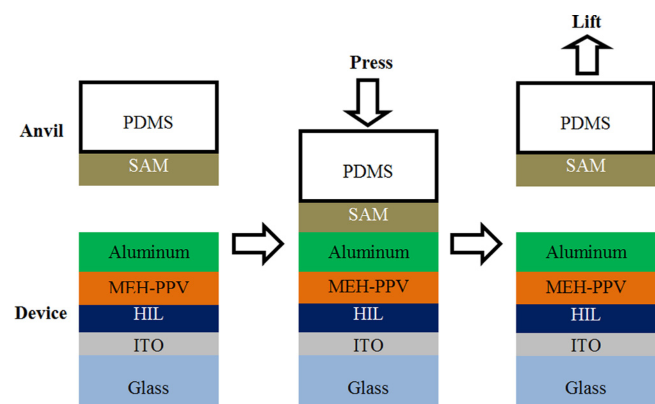

FIG. 1. Schematic of the pressure treatment for the pressure-assisted OLED fabrication process. The device was made with the MoO_3 or PEDOT:PSS as HIL material. The SAM coated anvil was pressed onto the device to add a pressure and then lifted from the device to remove the pressure.

 © 2014 AIP Publishing LLC

[This article is copyrighted as indicated in the article. Reuse of AIP content is subject to the terms at: http://scitation.aip.org/termsconditions. Downloaded to] IP: 64.54.217.125 On: Tue, 17 Jun 2014 17:57:03

luminance intensity and current efficiency, when compared with pressure-free diodes. This result was later confirmed by Fina *et al.*[11] Other researchers[12,13] have also reported improvements on the current density, photoluminescence, and electroluminescence, when pressure is applied to the OLEDs. Kim and Forrest[14] found that the pressures required to fabricate OLEDs could be 1000 times smaller when flexible polydimethylsiloxane (PDMS) stamps are used in cold welding processes instead of rigid silicon stamps. Cao *et al.*[15] have also used finite element simulations to show that, in cold welding processes, soft stamps are expected to deform easily around dust particles at relatively low pressures. However, considerably higher pressures are needed to deform stiff stamps over similar contact areas. In the case of lamination processes, the evolution of the contact profiles around dust particles has also been studied in our prior work,[16] in which numerical simulations were used to study the effects of pressure on conventional OLEDs that are relevant to displays.

In this study, OLEDs are fabricated with the novel hole-injection layer material, MoO_3. For comparison, they are also fabricated with a more conventional hole-injection layer material, PEDOT:PSS. Subsequently, the effects of pressure are studied by applying pressure to fabricated OLED structures with MoO_3 or PEDOT:PSS hole-injection layers. The current-voltage characteristics of both the MoO_3-based and PEDOT:PSS-based OLED structures are shown to be significantly improved by pressure treatment. Furthermore, in an effort to understand the underlying causes of the effects of pressure treatment, numerical finite element simulations are used to study the contacts between layers in the OLED structures. These utilize measurements of layer mechanical properties (Young's moduli and adhesion energies) that are obtained, respectively, using nanoindentation and atomic force microscopy techniques. These are incorporated into finite element models that were used for the simulation of the pressure-assisted OLED fabrication process. The models explore the effects of applied pressure on OLED structures with dust particles interposed between the hole-injection and emissive layers. They also show that pressure effects (on the electrical properties of OLEDs) can be explained by the increase in interfacial contact area that occurs under pressure. The implications of the current results are then discussed for the fabrication of robust and improved organic electronic devices.

II. PRESSURE-ASSISTED FABRICATION OF OLEDs

OLEDs with a traditional sandwich structure (Fig. 1) were fabricated at room temperature ($\sim$25 °C). The ITO-coated glass substrates (Delta Technologies, Stillwater, MN) were cleaned by sonication in methanol, acetone, and isopropyl alcohol for 30 min. The substrates were then further cleaned in an Ozone Ultraviolet Cleaner for 10 min (UVOCS, Lansdale, PA).

MoO_3 (Sigma-Aldrich, St. Louis, MO) was deposited on the cleaned ITO anode using an Edwards E306A thermal evaporation deposition system (Edwards, Sussex, UK). For comparison, another group of samples was fabricated with PEDOT:PSS, instead of MoO_3. Baytron P VP Al-4083 PEDOT:PSS (Heraeus Clevios, Hanau, Germany) was filtered through a 0.2 μm filter for 1 min at a rate of 3000 revolutions per minute (rpm) to further improve its smoothness and uniformity. Subsequently, the filtered solution was spin-coated onto the cleaned ITO anode at 1500 rpm for 15 s. The samples were then cured at 120 °C for 5 min to remove any residual moisture.

Poly[2-methoxy-5-(2′-ethyl-hexyloxy)-1,4-phenylene vinylene] (MEH:PPV) (Aldrich, St. Louis, MO), with molecular weight between 150 000 and 250 000, was used to form the emissive layer. It was dissolved in chloroform to produce a 5 mg/ml solution. After stirring the resulting solution for 6 h, it was filtered and then spin-coated onto the hole-injection layer at 800 rpm for 60 s. The aluminum cathode was thermally deposited onto the emissive layer using an Edwards E306A thermal evaporator (Edwards, Sussex, UK) operated at a vacuum of 10^{-7} Torr. The device area of 3 mm^2 was defined using conventional shadow masks. The resulting OLED structure had a pattern array of cylinders, with each cylinder having a radius of $\sim$0.98 mm and a distance of $\sim$4 mm between the centers of adjacent cylinders.

PDMS was used to prepare the anvil. The PDMS mixture (Sylgard 184, Dow Corning) was prepared by mixing a pre-polymer base with a curing agent. This was done in a 10:1 ratio (by weight) in a petri dish. The resulting mixture was then cured in a vacuum oven at 80 °C for 2 h. The cured PDMS anvil was then removed from the petri dish. On top of the PDMS anvil, a layer of (tridecafluoro-1,1,2,2,-tetrahydrooctyl)-trichlorosilane (Gelelest Inc., Morrisville, PA) was deposited as a self-assembled monolayer (SAM) that reduces the adhesion between the anvil and the device. The SAM was deposited by vapor deposition. This was done in a desiccator at room temperature ($\sim$25 °C) for 6 h.

The coated PDMS anvil was then brought into contact with the device using dead weight. This was used to apply a pressure between 5.6 MPa and 8.3 MPa to the fabricated OLEDs for 10 min at room temperature ($\sim$25 °C). Subsequently, the pressure was removed from the OLEDs by lifting up the anvil. It is important to note here that the SAM reduces the adhesion between the anvil and the device. This ensures that the anvil and the OLEDs are separated during the lifting stages.

Electrical characterization of the OLEDs was also carried out before and after pressure treatment. This was done using a Keithley 2400 broad purpose source meter (Keithley Instruments, Inc., Cleveland, Ohio). The source meter was connected to the OLEDs such that current was sourced in the sweep mode between 0 and 20 mA with a delay of 500 ms. This specified forward bias current applied in the sweep mode with a corresponding working turn-on voltage is being recorded, resulting in current-voltage (J-V) data sets.

The fabrication and characterization of the OLEDs were all carried out in an ISO Class 7 clean room environment according to the ISO 14644-1 standards.[17]

III. EXPERIMENTAL METHODS

A. Nanoindentation

Since the mechanical properties of thermally deposited MoO_3 layers have not been well characterized in the literature,

[This article is copyrighted as indicated in the article. Reuse of AIP content is subject to the terms at: http://scitation.aip.org/termsconditions. Downloaded to] IP: 64.54.217.125 On: Tue, 17 Jun 2014 17:57:03

nanoindentation experiments were used to measure the Young's modulus of MoO_3. First, the MoO_3 (Sigma-Aldrich, St. Louis, MO) was deposited onto the surface of glass slides by thermal evaporation. This was done using an Edwards E306A thermal evaporator deposition system (Edwards, Sussex, UK). The resulting MoO_3 thin films had thicknesses of around 25 nm, as measured using a KLA-Tencor P15 Surface Profiler (KLA-Tencor, Milpitas, CA).

Nanoindentation measurements were then carried out on the MoO_3 thin films. The experiments were performed with a TriboScope nanomechanical testing system (Hysitron Inc., Minneapolis, MN), coupled to a Dimension 3100 scanning probe microscope (Veeco Instruments Inc., Woodbury, NY). A Berkovich indenter tip, a three sided pyramidal-type tip, with an included angle of 142.3°, was used for nanoindentation. This was chosen for its large angle, hence large contact area, with the samples. The loading profile consisted of the following three steps: Loading to a peak load in 2 s; holding at the peak load for 2 s, and returning to zero load in 2 s. A peak load ranging from 60 μN to 200 μN was applied. To minimize the possible interactions between adjacent indents, all the indents were separated by at least 20 μm. Images of the surfaces (before and after the indentation) were obtained using a contact-based scanning probe technique.

The indentation depths were generally much greater than the surface roughness levels. Commonly, for metallic materials, indentation depths should be at least 20 times greater than the average surface roughness to minimize the possible effects of rough surfaces.[18] Also, the indentation depths should be less than 10% of the film thickness to minimize substrate effects.[19] This is especially true for films that are much harder than the substrate. In this study, a range of peak loads was selected, which generated a range of contact depths during the indentation experiments. These were used to study the possible effects of indentation depth. Finally, the peak loads were maintained for sufficient durations to minimize the possible effects of viscoelasticity on the measured Young's moduli.

B. AFM adhesion measurements

AFM adhesion measurements were used to study the adhesion between the hole-injection layer and the emissive layer, i.e., between MoO_3 and MEH-PPV. As a more conventional hole-injection layer material, PEDOT:PSS was studied for comparison. The adhesion between PEDOT:PSS and MEH-PPV was also measured.

The filtered PEDOT:PSS solution, described above, was spin-coated onto glass slides and then cured. The filtered MEH-PPV solution, described above, was also spin-coated onto other glass slides. Using a Dimension 3000 AFM (Digital Instruments, Plainview, NY) under tapping mode, the root mean square surface roughness of each film was measured from the surface profile.

Etched silicon contact AFM tips (Veeco Instruments, Woodbury, NY) were coated with MoO_3 (Sigma-Aldrich, St. Louis, MO) using the same thermal evaporator described earlier. The AFM tips were also coated with the same filtered MEH-PPV solution described above. This was done using a dip-coating technique developed in prior studies by Wolf *et al.*[20] After coating, scanning electron microscopy (SEM) images were obtained in a FEI XL30 FEG-SEM (Philips, Hillsboro, OR). These were used to validate the coating and measure the AFM tip radii from the tip profile.

Contact AFM experiments were performed using the MoO_3 coated tips and the MEH-PPV substrates. They were also performed using the MEH-PPV coated tips and PEDOT:PSS substrates. The experiments were performed in air, over a temperature range of 22–25 °C and relative humidity range of 31%–46%. At least six force-displacement curves were obtained for each interaction, using the same Dimension 3000 AFM described earlier. These were used to measure the deflection of the AFM tips, as they were pulled off from the substrate. The spring constants of each tip were measured using the thermal tune method.[21] This was done using a Nanoscope IIIa AFM (Digital Instruments, Plainview, NY). By substituting the spring constant and the measured deflections into Hooke's Law, the adhesion forces were estimated for the interfaces between the coated tips and the substrates.

IV. MODELING

A. Adhesion models

There are several existing models describing the adhesion interaction between two spheres. To select the appropriate model, Maugis[22] defined a transition parameter, λ, which is given by

$$\lambda = 2\sigma_0\left(\frac{R}{\pi\kappa^2\gamma}\right)^{1/3}, \quad (1)$$

where γ is the adhesion energy per unit area; R is the combined radius given by $R = R_1R_2/(R_1 + R_2)$, where R_1 and R_2 are the radii of the two spheres, respectively; κ is the combined elastic modulus for two spheres in contact, which is given by $\kappa = 4/3[(1-\nu_1)^2/E_1 + (1-\nu_2)^2/E_2]$, where E_1 and E_2 are the elastic moduli of the two spheres, and ν_1 and ν_2 are the Poisson's ratios of the two spheres, respectively. By choosing σ_0 to match the minimum adhesive stress of a Lennard–Jones potential with equilibrium separation distance z_0, it follows that $\delta_0 = 0.97z_0$. The Johnson–Kendall–Roberts (JKR) model[23] applies when $\lambda > 5$. The Derjaguin–Muller–Toporov (DMT) model[24] applies when $\lambda < 0.1$. The Maugis–Dugdale (MD) model[22] applies for the intermediate values of λ.

For the two extreme cases, the adhesion energy is given in JKR and DMT theories by

$$\gamma_{JKR} = \frac{2F_{ad}}{3\pi R}, \quad (2)$$

$$\gamma_{DMT} = \frac{F_{ad}}{2\pi R}, \quad (3)$$

where F_{ad} can be the adhesion force measured by the AFM adhesion experiments.

For MD model, the calculation was simplified using an iterative process, introduced by Carpick *et al.*[25] and further

[This article is copyrighted as indicated in the article. Reuse of AIP content is subject to the terms at: http://scitation.aip.org/termsconditions. Downloaded to] IP: 64.54.217.125 On: Tue, 17 Jun 2014 17:57:03

developed by Piétrement and Troyon.[26] Another dimensionless parameter α was defined and calculated through curve fitting to be

$$\lambda = -0.913 \ln(1 - 1.018\alpha). \tag{4}$$

A dimensionless adhesion force was defined by

$$\hat{F}_{ad} = \frac{F_{ad}}{\pi \gamma R}. \tag{5}$$

They also determined empirical equations supplying direct conversion equations between parameter α and $\hat{F}_{ad}$ by

$$\hat{F}_{ad} = 0.267\alpha^2 - 0.767\alpha + 2.000. \tag{6}$$

The AFM force measurement measures F_{ad}. With R and κ known, the adhesion energy can be calculated by solving the Eqs. (1) and (4)–(6).

The adhesion theories mentioned above have been used in other studies[27–29] to calculate the adhesion energy from the AFM force measurements.

B. Analytical models of pressure-free contact profile

Dust particles in the typical semiconductor clean room environment include silicon, iron, aluminum, quartz, textile polymer, silicone, and photoresist.[15] The typical airborne dust particle diameter ranges from ~0.1 to 20 μm.[17,30] During the fabrication of organic electronic devices, the dust particles are interposed between the layers in the devices. They, therefore, affect the evolution of contact areas between adjacent layers. It is important to note here, that prior work[31] has used transmission electron microscopy and electron energy loss spectroscopy to reveal dust particles and interfacial gaps between both cold-welded interfaces and the electron-beam evaporated interfaces.

Several analytical models[32,33] are relevant to the study of contact profile of the initial interfaces around the dust particles before pressure treatment. Considering the model of a membrane suspended on top of a particle, a blister forms under the suspended beam, with a radius, a. Malyshev and Salganik[32] have solved the problem of the classical penny crack under a plate in bending. According to them, the relationship between the adhesion energy and the contact profile can be represented by

$$\gamma = \frac{2Et^3h^2}{3(1-\nu^2)a^4}, \tag{7}$$

where E and ν are the Young's modulus and Poisson's ratio of the membrane material, respectively; t is the thickness of the membrane; and h is the height of the blister under the beam, which is equal to the diameter of the interposed particle.

If the thickness of the suspended membrane is much smaller than the height and the radius of the blister, then membrane stretching dominates the mechanical energy instead of membrane bending. Under such conditions, Wan and Mai[33] have shown that the adhesion energy between the membrane and the substrate is given by

$$\gamma = \frac{Eth^4}{16a^4}. \tag{8}$$

This model has been used to describe the contact profile of graphene sheets around silver particles on silicon substrates.[34]

C. Finite element simulations

Cao et al.[15] have studied the evolution of contact areas between layers that are relevant to cold welding processes. The evolution of the contact area has also been investigated for lamination processes in our previous work.[16] Hence, as an extension of prior work, this paper examines the effects of pressure on contact profiles of OLED structures with improved MoO_3 hole-injection layers that are deposited by thermal evaporation. Finite element simulations of the effects of pressure treatment were carried out using the Abaqus software package (Dassault Systèmes Simulia Corporation, Providence, RI). The effects of the dust particles were considered in the simulations of contact between hole-injection layer (MoO_3 or PEDOT:PSS) and the emissive layer (MEH-PPV).

The simulations considered the parts of the devices in the vicinity of dust particles. Axisymmetric geometries were used to simplify the cylindrical geometry of the structure. The simulated part of the structure has a radius of 200 μm. Also, the thicknesses of the simulated portions of the PDMS stamp and the glass substrate were all 200 μm. It was assumed that the other part of the device, which is further away from the dust particle, has a negligible effect on the mechanics around the dust particle.

A typical finite element model is presented in Fig. 2. It shows a PDMS stamp about to compress onto an evaporated device. Note that the material of each layer is marked in the figure. The HIL material could be either MoO_3 or PEDOT:PSS. The layer thicknesses are 200 nm, 100 nm, 50 nm, and 200 nm for aluminum, MEH-PPV, HIL, and ITO, respectively. It has been shown by Moreau[17,30] that the diameter of airborne dust particles in a typical semiconductor clean room environment ranges from ~0.1 to 20 μm. The particles smaller than 0.1 μm increase in size through

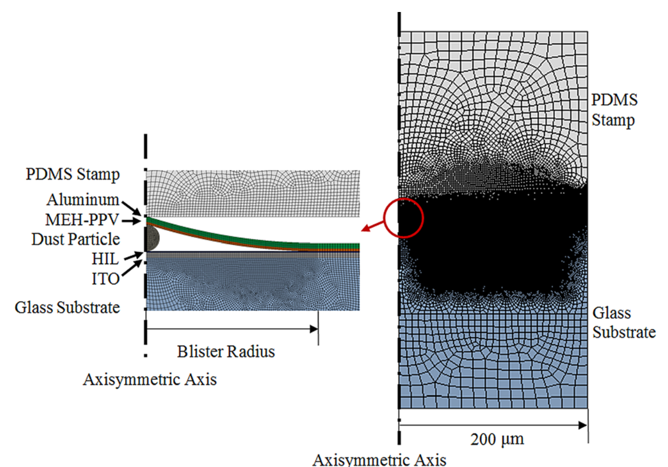

FIG. 2. FEA Model for the pressure treatment in the pressure-assisted fabrication of OLEDs. The HIL material could be either MoO_3 or PEDOT:PSS.

[This article is copyrighted as indicated in the article. Reuse of AIP content is subject to the terms at: http://scitation.aip.org/termsconditions. Downloaded to] IP: 64.54.217.125 On: Tue, 17 Jun 2014 17:57:03

TABLE I. Material properties used in the finite element simulations.

Material	Young's modulus (GPa)	Poisson's ratio	Reference
PDMS	0.003	0.48	35 and 36
Aluminum	70	0.3	37
PEDOT:PSS	1.42	0.3	16
MoO_3	64.6	0.3	Current study
MEH-PPV	11.5	0.3	16
ITO	116	0.35	38
Glass	69	0.3	37
Particle	70	0.3	15

agglomeration. The particles greater than 10 μm settle rapidly. Most of the airborne migrating particles have a diameter of 1 μm. Therefore, the diameter of dust particle was chosen to be 1 μm in the calculation. The radius of the blister was calculated using analytical models described earlier in this work (Sec. IV B).

A 4-node bilinear axisymmetric quadrilateral element was used in the mesh. The mesh was dense in the regions near the dust particle and the contact surfaces. Similar mesh sizes were also used in the regions near the surface contact regimes to assure convergence in contact simulation. It was assumed that all the materials exhibited isotropic elastic behavior. Young's moduli were obtained from the nanoindentation experiments described earlier in this work as well as from prior studies.[15,16,35–38] The Young's moduli and the Poisson's ratios of the materials used in the simulations are summarized in Table I. The Young's moduli of the various dust particles that are found in a typical semiconductor clean room environment are summarized in Table II. The low moduli of soft dust particles suggest that they will spread along the interface, and hence do not lead to significant pressure effect. Considering that the hard particles play a dominant role in controlling the contact area, a Young's modulus of 70 GPa was used for the calculation.[15]

The axisymmetric boundary condition was applied at the symmetry axis (Fig. 2). The bottom of the substrate was fixed to have no displacements and rotations. The outer edge of the model was also fixed to have no lateral movement for continuity. The top of the stamp moved downward. A pressure was applied from the stamp onto the device. For simplicity and for convergence, frictionless contact was assumed between contact surfaces.

TABLE II. Young's moduli of dust particles in a typical semiconductor clean room environment, adapted from Ref. 15.

Material	Young's modulus (GPa)	Reference
Silicon	75–200	40 and 42
Iron	196	37
Aluminum	70	37
Quartz	70–94	37 and 43
Textile polymer	1–5	44
Silicone	0.001–0.02	35, 36, and 45
Photoresist	1–8	37, 42, and 46

V. RESULTS AND DISCUSSION

A. Electrical characterization of OLEDs

The current-voltage characteristics obtained for the OLEDs (both before and after the pressure treatments) are presented in Figs. 3(a) and 3(b), for the MoO_3-based and PEDOT:PSS-based devices, respectively. Each line is an average of the electric characterization results for three devices. These show that the current density, for a given voltage, increases with applied pressure. This is true for both MoO_3-based and PEDOT:PSS-based devices. The results also show that the applied pressure causes the threshold voltage to decrease from $\sim$10 V to $\sim$6 V in the case of the PEDOT:PSS-based devices. In the case of the OLEDs with the MoO_3 hole-injection layers, the threshold voltage was $\sim$5 V in a device that was fabricated without the application of pressure. This is significantly lower than the threshold voltage of $\sim$10 V in OLEDs with the PEDOT:PSS HIL. The threshold voltage was further reduced to $\sim$2 V, following the application of the pressure to the OLEDs with the MoO_3 hole-injection layer, as shown in Fig. 3(b).

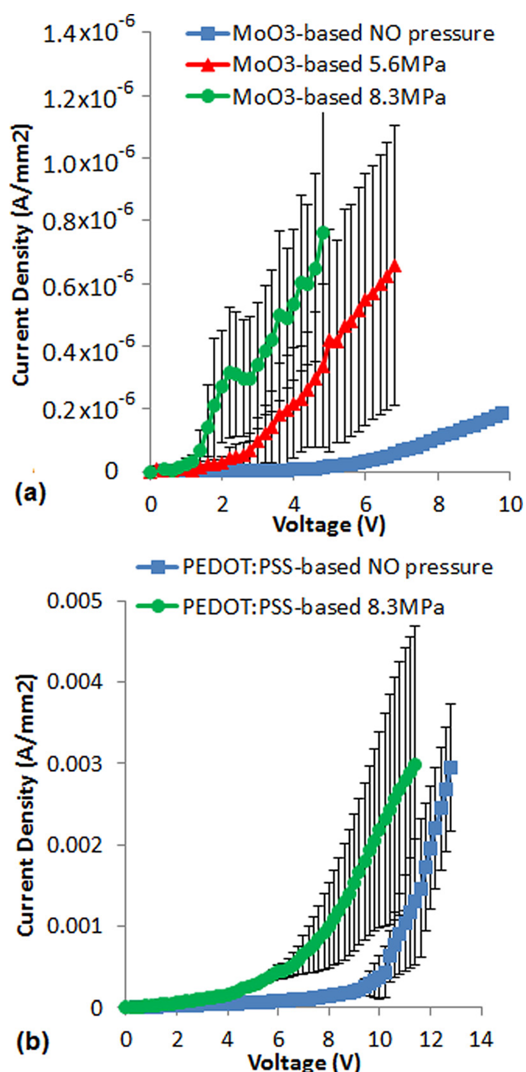

FIG. 3. Current-voltage characteristic for (a) MoO_3-based devices and (b) PEDOT:PSS-based devices before and after pressure treatment.

[This article is copyrighted as indicated in the article. Reuse of AIP content is subject to the terms at: http://scitation.aip.org/termsconditions. Downloaded to] IP: 64.54.217.125 On: Tue, 17 Jun 2014 17:57:03

The dispersions between each device are described by the error bars in Fig. 3. The pressure is applied on the devices using dead weight. The dispersion could be caused by the unevenly distributed pressure or the impact force. It could be reduced by better control of the applied pressure using an mechanical testing machine, such as Instron machine.

Furthermore, there is a need for long-term studies of the long-term stability of the OLEDs made with pressure-facilitated fabrication method. Such studies are needed to ensure that the applied pressure does not degrade the long-term performance and stability of the resulting OLEDs. They are recommended for future work.

B. Nanoindentation and Young's modulus

Typical scans of the MoO_3 thin film surfaces, obtained before and after indentation, are presented in Fig. 4. In some materials, the volume under the indenter pushes out into the sides of the indenter during the indentation to form a pile-up profile. In those cases, the actual contact depth may be larger than the measured contact depth.[39] The image Fig. 4 shows that there is no significant pile-up during the indentation of MoO_3 thin films.

The reduced Young's moduli and hardness values (obtained over a range of contact depths) are summarized in Fig. 5. The results suggest that there is no strong correlation between the contact depth and the reduced Young's modulus or hardness. The reduced Young's modulus and hardness of MoO_3 were measured to be 66.8 ± 6.1 GPa and 2.6 ± 0.7 GPa, respectively. Hence, the Young's modulus of MoO_3 was determined to be 64.6 ± 6.2 GPa, assuming that the Poisson's ratio is 0.3. The measured root-mean-squared surface roughness for the MoO_3 substrate before indentation is 0.7 ± 0.3 nm. The measured indentation depth (at a range of 9 to 22 nm) is enough to overcome the effects of surface roughness.[18] The measured Young's modulus of MoO_3 is smaller than that of the glass substrate, which is 70 GPa.[37] The results also show that the substrate effects are negligible when the modulus of the coating is smaller than that of the substrate, since the plastic deformation is constrained in the coating layer, as suggested in prior work by Saha and Nix.[40]

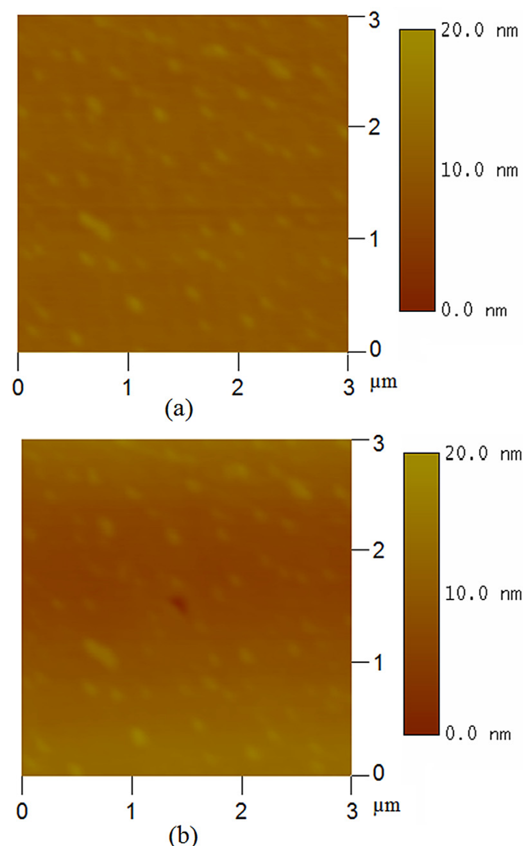

FIG. 4. Typical surface profiles of MoO_3 thin film (a) before and (b) after nanoindentation measurement.

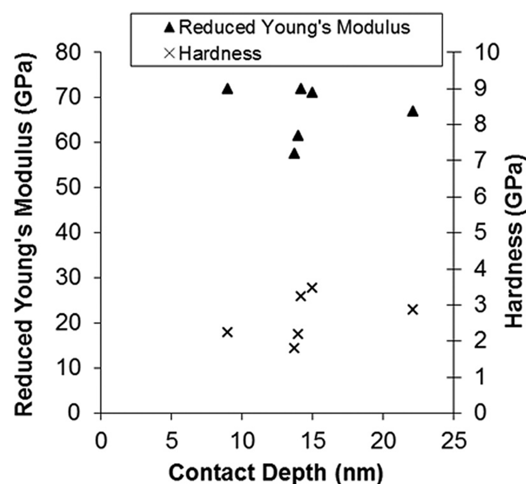

FIG. 5. Reduced Young's modulus and hardness of MoO_3 thin film measured by nanoindentation.

C. Adhesion measurements and adhesion energies

The tip radii of the MoO_3-coated AFM tips were measured to be 157.5 nm from the SEM images. The root mean squared surface roughness of MEH-PPV substrates was measured from the surface profile obtained from AFM tapping scans to be 2.2 ± 0.7 nm. Contact AFM experiments were performed using the MoO_3 coated tips and the MEH-PPV substrates. The pull-off force measured by AFM was 31.8 ± 7.8 nN.

Also, the contact AFM experiments were performed using the MEH-PPV coated tips and PEDOT:PSS substrates. The tip radii of the MEH-PPV coated tip were measured to be 222 nm from the SEM images. The root-mean-squared surface roughness of PEDOT:PSS substrate was measured from the AFM surface profile to be 0.6 ± 0.1 nm. The pull-off force between the MEH-PPV coated tips and the PEDOT:PSS substrates was measured to be 59.3 ± 8.4 nN.

The Young's modulus of MoO_3 was measured to be 64.6 GPa in this study. The Young's modulus of MEH-PPV was measured to be 11.5 GPa in prior studies.[16] The combined elastic modulus was calculated, assuming that the Poisson's ratios of MoO_3 and MEH-PPV were both 0.3. The combined radius was then calculated by assuming the substrate is a flat surface with an infinitely large radius, since the surface roughness of the substrate, 2.2 nm, is much smaller than the radius of the tip, 157.5 nm. The transition parameter,

[This article is copyrighted as indicated in the article. Reuse of AIP content is subject to the terms at: http://scitation.aip.org/termsconditions. Downloaded to] IP: 64.54.217.125 On: Tue, 17 Jun 2014 17:57:03

λ, was calculated to be in the intermediate range, where the MD model applies. The adhesion energy was determined to be 0.0398 J/m^2. This was determined by numerically solving Eqs. (1) and (4)–(6).

In the case of the adhesion interaction between PEDOT:PSS and MEH-PPV, the Young's moduli were measured in a previous study[16] to be 1.42 GPa and 11.5 GPa, respectively. The combined elastic modulus was calculated, assuming that the Poisson's ratios of both materials were both equal to 0.3. The combined radius was determined by assuming the substrate is a flat surface with an infinitely large radius, since the surface roughness of the substrate, 0.6 nm, is much smaller than the radius of the tip, 222 nm. The transition parameter, λ, was calculated to be greater than 5. Thus, the JKR model applies. Hence, the adhesion energy was calculated by JKR model from Eq. (2) to be 0.0567 J/m^2.

D. Evolution of contact profiles under pressure

Several analytical models[32,33] are relevant to the contact profiles between thin layers. Also, most of the dust particles in the clean room environment have diameters of $\sim$1 μm.[30] Since thickness of the emissive layer is $\sim$100 nm, which is much smaller than the height of the blister, i.e., the diameter of the dust particle, stretching dominates the strain energy and the membrane stretching model applies.[33] By substituting the adhesion energy measured previously (Sec. V C), the radius of the blister between the emissive layer and the hole-injection layer was calculated from Eq. (8) to be 6.52 μm for MoO_3-based OLEDs and 5.97 μm for PEDOT:PSS-based OLEDs, before the application of pressure.

The calculated initial blister radius was incorporated into the finite element models for the simulation of contact profile evolution under pressure via the PDMS stamps. A typical calculated profile of a stamp on a MoO_3-based device (under 14 MPa pressure) is presented in Fig. 6(a). The stamp has clearly deformed under pressure and made full contact with the top of the device. Being compressed by the stamp, the top of the blister deformed and made contact with the substrate HIL. The radius of the blister decreased, since part of the internal surfaces of the blister made contact under pressure. Due to adhesion, the contacted internal surface of the blister remains in contact after the pressure is removed. The radius and the area of the blister can be used to characterize the efficiency of the pressure treatment.

It is also important to note that Fig. 6(a) also shows that the dust particle indent into the substrate HIL, due to the applied pressure. Hence, the lowest point of the substrate surface was right beneath the dust particle, while the highest point of the substrate was at the edge of the model. The height difference between the highest and lowest points was defined as the sink-in depth. This was used to characterize the damage to the device.

The blister radius and area both decreased with increasing pressure, for either MoO_3-based or PEDOT:PSS-based device, as shown in Fig. 6(b). However, the rate of decrease of blister radius and the area decreased at higher pressures. This was especially true when the pressure was greater than 8 MPa. The blister radius and area are normalized in Fig. 6(c). This shows

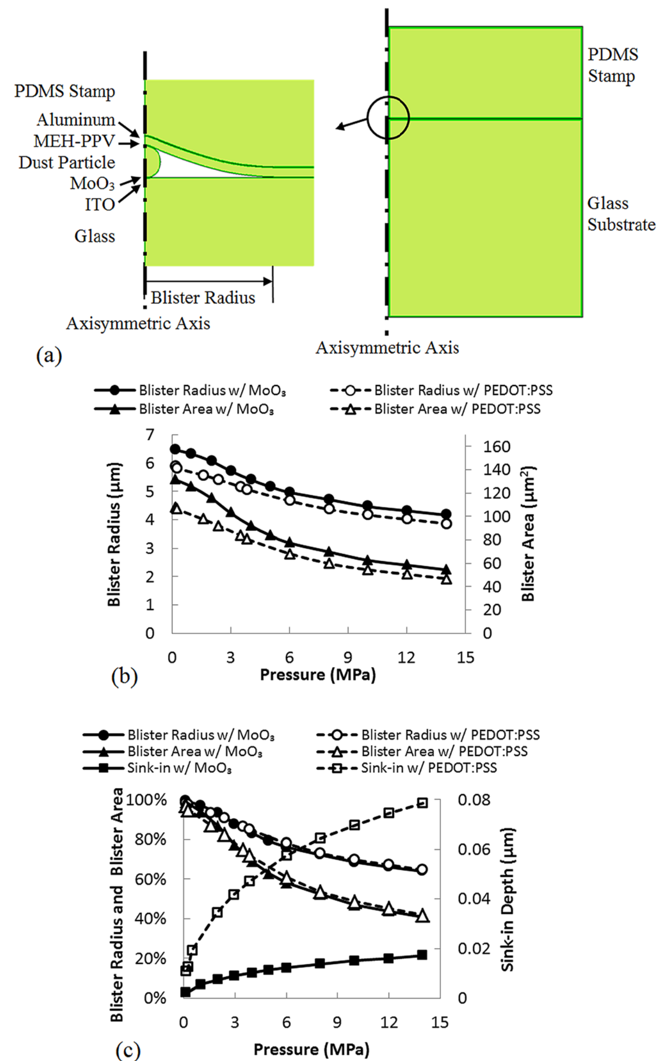

FIG. 6. FEA simulation results of (a) predicted contact profile of MoO_3-based device under 14 MPa pressure, (b) the evolution of blister morphology during the pressure treatment, and (c) the normalized blister morphology.

that the normalized blister radius and area, for MoO_3-based and PEDOT:PSS-based device, exhibit a similar trend of evolution under pressure. The blister area for both the MoO_3-based and PEDOT:PSS-based devices decreased to $\sim$60% of their initial values when the applied pressure reached 5.6 MPa. Also, the blister area further decreased to $\sim$50% of its initial value, when the applied pressure reached 8.3 MPa.

Fig. 6(c) also shows that the sink-in depth increased under pressure. The rate of increase also decreased under pressure. It is important to note here that the MoO_3 and PEDOT:PSS layers have the same initial thickness in the simulation. However, the sink-in depth into the MoO_3 layer is $\sim$4 times smaller than that into the PEDOT:PSS layer. This is because the Young's modulus of MoO_3 is much greater than that of PEDOT:PSS. This suggest that the MoO_3-based device is likely to be more resistant to damage than OLEDs with more compliant PEDOT:PSS hole-injection layers.

In the above analysis, the calculated results were obtained from a model with a dust particle diameter of 1 μm. The diameter was chosen as a representative diameter for airborne migrating particles in a typical semiconductor clean

[This article is copyrighted as indicated in the article. Reuse of AIP content is subject to the terms at: http://scitation.aip.org/termsconditions. Downloaded to] IP: 64.54.217.125 On: Tue, 17 Jun 2014 17:57:03

room environment.[17,30] Also, the Young's modulus of the dust particle that was used in the model is 70 GPa. This was selected because it is representative of hard particles, such as glass, that have a dominant pressure effect on the contact profile. The modeling of different specific particles with a range of diameters and specific Young's moduli is recommended as an area for future work.

E. Implications

This study shows clearly that the threshold voltages of OLEDs are improved by pressure application and improved hole-injection layers. The effects of pressure are attributed to the closing up of voids or the corresponding increase in the contact lengths. In any case, the contact lengths increase under pressure, while the void lengths decrease under pressure, resulting in increased contact area across the interfaces in the OLED structures. Hence, the lower threshold voltages in the OLEDs that were fabricated using pressure-assisted processes are attributed largely to the increased contact area due to the application of pressure.

Hence, the current work suggests that the current-voltage characteristics of OLEDs can be enhanced by the application of controlled levels of pressure in lamination/-stamping processes. Such pressure may be applied after using conventional spin-coating and thermal evaporation techniques to deposit the individual layers in the OLED structures. However, great care is needed to ensure that the applied pressure does not result in excessive sink-in, which can lead to damage of the device. The required balance of improved contact without excessive sink-in should also be guided by computational models and some experiments.

It is also important to note that significant improvements in OLED performance were also associated with the use of molybdenum trioxide as an improved hole-injection layer. However, further work is clearly needed to explore the potential of other transition metal oxides as hole-injection layers in organic light emitting devices. These include: WO_3, NiO, or V_2O_5, that have been shown to have the potential to effectively replace PEDOT:PSS in OLEDs,[4–6] OPV cells,[2,7] and OTFTs.[8]

There is also a need to explore a range of deposition methods for the fabrication of organic layers in polymer-based devices. These include spin-coating and thermal evaporation techniques that must be optimized prior to pressure-assisted fabrication. Such developments could facilitate the development of fast, low-cost stamping and roll-to-roll processes[41] for the fabrication of organic light emitting devices. The current work suggests that these are possible, provided sufficient pressures are applied, without inducing significant damage (sink-in) in the layered structures of the devices.

VI. SUMMARY AND CONCLUDING REMARKS

This paper presents the results of a combined experimental, theoretical, and computational study of the pressure-facilitated fabrication of OLEDs. The OLEDs were fabricated using a novel HIL material, MoO_3, and the more conventional material, PEDOT:PSS. The current-voltage characteristics of the devices were measured before and after the pressure treatment. The results showed a dramatic decrease of the threshold voltage after the application of pressure. This was true for both the MoO_3-based and PEDOT:PSS-based devices. In order to study the mechanism of the pressure effects, the nanoindentation method and AFM techniques were used, respectively, to measure the key mechanical properties (Young's moduli and hardness values) and adhesion energies of the layers and interfaces. The measured properties were then incorporated into analytical models for the calculation of the contact profiles around dust particles interposed between the HIL and EML. A finite element model was used to simulate the evolution of contact profile under pressure. The results suggest that the application of pressure, to the evaporated or spin-coated device layers, reduces the blister area surrounding the interposed dust-particle. This increases the contact area between the HIL and EML. Since such significant increase in the contact area would facilitate charge transport across interfaces in the OLED structures, we attribute the reduction of the threshold voltages of the pressure-assisted devices to the improvement of the charge transport across interfaces with increased contacts. However, it is important to note that excessive lamination pressure may also induce device damage due to the sink-in of dust particles. This suggests the need to optimize the pressure for improved surface contact without significant damage.

ACKNOWLEDGMENTS

The research was support by grants from the National Science Foundation, the Princeton Environmental Institute, the Andlinger Center, and the STEP B Program of the World Bank, the African Centers of Excellence (ACE) Program of the World Bank, the African Development Bank and the Nelson Mandela Institution. The authors are also grateful to Mr. Joseph Palmer for his technical assistance at the Princeton Institute of Science and Technology of Materials (PRISM).

[1]T.-W. Lee, J. Zaumseil, Z. Bao, J. W. P. Hsu, and J. A. Rogers, Proc. Natl. Acad. Sci. U.S.A. **101**, 429–433 (2004).
[2]V. Shrotriya, G. Li, Y. Yao, C.-W. Chu, and Y. Yang, Appl. Phys. Lett. **88**, 073508 (2006).
[3]J. Meyer, K. Zilberberg, T. Riedl, and A. Kahn, J. Appl. Phys. **110**, 033710 (2011).
[4]K. J. Reynolds, J. A. Barker, N. C. Greenham, R. H. Friend, and G. L. Frey, J. Appl. Phys. **92**, 7556 (2002).
[5]H. You, Y. Dai, Z. Zhang, and D. Ma, J. Appl. Phys. **101**, 026105 (2007).
[6]W.-J. Shin, J.-Y. Lee, J. C. Kim, T.-H. Yoon, T.-S. Kim, and O.-K. Song, Org. Electron. **9**, 333–338 (2008).
[7]Y.-C. Tseng, A. U. Mane, J. W. Elam, and S. B. Darling, Sol. Energy Mater. Sol. Cells **99**, 235–239 (2012).
[8]C.-W. Chu, S.-H. Li, C.-W. Chen, V. Shrotriya, and Y. Yang, Appl. Phys. Lett. **87**, 193508 (2005).
[9]J. Meyer, A. Shu, M. Kröger, and A. Kahn, Appl. Phys. Lett. **96**, 133308 (2010).
[10]J. H. Kim, S. Seo, and H. H. Lee, Appl. Phys. Lett. **90**, 143521 (2007).
[11]M. Fina, D. Liu, L. Ren, and S. S. Mao, Appl. Phys. A **105**, 323–327 (2011).
[12]X. Fan, J. Sun, F. Wang, Z. Chu, P. Wang, Y. Dong, R. Hu, B. Z. Tang, and D. Zou, Chem. Commun. **2008**, 2989–2991 (2008).
[13]Z. Y. Jiang and X. A. Cao, Appl. Phys. Lett. **97**, 203304 (2010).
[14]C. Kim and S. Forrest, Adv. Mater. **15**, 541–545 (2003).
[15]Y. Cao, C. Kim, S. R. Forrest, and W. Soboyejo, J. Appl. Phys. **98**, 033713 (2005).
[16]J. Du, T. Tong, W. Akande, A. Tsakiridou, and W. Soboyejo, J. Disp. Technol. **9**, 601–606 (2013).

[This article is copyrighted as indicated in the article. Reuse of AIP content is subject to the terms at: http://scitation.aip.org/termsconditions. Downloaded to] IP: 64.54.217.125 On: Tue, 17 Jun 2014 17:57:03

[17]International Organization for Standardization, ISO 14644-1:1999, *Cleanrooms of and Associated Controlled Environments-Part 1: Classification of Air Cleanliness* (ISO, Switzerland, 1999).
[18]International Organization for Standardization, ISO 14577-1:2002, *Metallic Materials, Instrumented Indentation Test for Hardness and Materials Parameters—Part 1: Test Method* (ISO, 2002).
[19]W. C. Oliver and G. M. Pharr, J. Mater. Res. **7**, 1564–1583 (1992).
[20]K. V. Wolf, Z. Zong, J. Meng, A. Orana, N. Rahbar, K. M. Balss, G. Papandreou, C. A. Maryanoff, and W. Soboyejo, J. Biomed. Mater. Res. A **87A**, 272–281 (2008).
[21]F. M. Serry, *Improving the Accuracy of AFM Force Measurements: The Thermal Tune Solution to the Cantilever Spring Constant Problem* (Veeco Instruments Inc., Santa Barbara, 2005), pp. 1–4.
[22]D. Maugis, J. Colloid Interface Sci. **150**, 243–269 (1992).
[23]K. L. Johnson, K. Kendall, and A. D. Roberts, Proc. R. Soc. A Math. Phys. Eng. Sci. **324**, 301–313 (1971).
[24]B. V. Derjaguin, V. M. Muller, and Y. P. Toporov, J. Colloid Interface Sci. **53**, 314–326 (1975).
[25]R. Carpick, D. Ogletree, and M. Salmeron, J. Colloid Interface Sci. **211**, 395–400 (1999).
[26]O. Piétrement and M. Troyon, J. Colloid Interface Sci. **226**, 166–171 (2000).
[27]T. Tong, B. Babatope, S. Admassie, J. Meng, O. Akwogu, W. Akande, and W. O. Soboyejo, J. Appl. Phys. **106**, 083708 (2009).
[28]N. Rahbar, K. Wolf, A. Orana, R. Fennimore, Z. Zong, J. Meng, G. Papandreou, C. Maryanoff, and W. Soboyejo, J. Appl. Phys. **104**, 103533 (2008).
[29]J. Meng, E. Paetzell, A. Bogorad, and W. O. Soboyejo, J. Appl. Phys. **107**, 114301 (2010).
[30]W. M. Moreau, *Semiconductor Lithography: Principles, Practices, and Materials* (Plenum Press, New York, 1988).
[31]W. O. Akande, Y. Cao, N. Yao, and W. Soboyejo, J. Appl. Phys. **107**, 043519 (2010).
[32]B. M. Malyshev and R. L. Salganik, Int. J. Fract. **26**, 261–275 (1984).
[33]K. Wan and Y. Mai, Int. J. Fract. **74**, 181–197 (1995).
[34]Z. Zong, C.-L. Chen, M. R. Dokmeci, and K. Wan, J. Appl. Phys. **107**, 026104 (2010).
[35]A. Bietsch and B. Michel, J. Appl. Phys. **88**, 4310 (2000).
[36]N. Bowden, S. Brittain, A. G. Evans, J. W. Hutchinson, and G. M. Whitesides, Nature **393**, 146 (1998).
[37]W. Soboyejo, *Mechanical Properties of Engineered Materials* (CRC, New York, 2003).
[38]D. Neerinck and T. J. Vink, Thin Solid Films **278**, 12–17 (1996).
[39]W. C. Oliver and G. M. Pharr, J. Mater. Res. **19**, 3–20 (2004).
[40]R. Saha and W. D. Nix, Acta Mater. **50**, 23–38 (2002).
[41]S. R. Forrest, Nature **428**, 911–918 (2004).
[42]M. Gad-el-Hak, *The MEMS Handbook* (CRC Press, New York, 2002).
[43]M. T. Kim, Thin Solid Films **283**, 12–16 (1996).
[44]W. D. Callister, *Materials Science and Engineering: An Introduction* (Wiley, New York, 2003).
[45]H. Schmid and B. Michel, Macromolecules **33**, 3042–3049 (2000).
[46]C. Kim, Y. Cao, W. O. Soboyejo, and S. R. Forrest, J. Appl. Phys. **97**, 113512 (2005).

[This article is copyrighted as indicated in the article. Reuse of AIP content is subject to the terms at: http://scitation.aip.org/termsconditions. Downloaded to] IP: 64.54.217.125 On: Tue, 17 Jun 2014 17:57:03